Journal of Catalysis 365 (2018) 292–302

Contents lists available at ScienceDirect

Journal of Catalysis

journal homepage: www.elsevier.com/locate/jcat

The role of Bi-doping in promoting electron transfer and catalytic performance of Pt/3DOM-$Ce_{1-x}Bi_xO_{2-\delta}$

Kai Yu [a,b,c], Da Lei [a,b], Yajun Feng [a], Haochen Yu [b], Yue Chang [b], Yanbing Wang [b], Yaqi Liu [a], Gui-Chang Wang [d], Lan-Lan Lou [b,c,*], Shuangxi Liu [b,*], Wuzong Zhou [c,*]

[a] MOE Key Laboratory of Pollution Processes and Environmental Criteria, College of Environmental Science and Engineering, Nankai University, Tianjin 300350, China
[b] Institute of New Catalytic Materials Science and MOE Key Laboratory of Advanced Energy Materials Chemistry, School of Materials Science and Engineering, National Institute of Advanced Materials, Nankai University, Tianjin 300350, China
[c] School of Chemistry, University of St Andrews, St Andrews, Fife KY16 9ST, United Kingdom
[d] College of Chemistry, Nankai University, Tianjin 300071, China

ARTICLE INFO

Article history:
Received 25 April 2018
Revised 25 June 2018
Accepted 26 June 2018

Keywords:
Asymmetric oxygen vacancy
Electron transfer
Promoting mechanism
Aerobic oxidation
5-Hydroxymethyl-2-furfural

ABSTRACT

Investigation of Bi-doping effects on the catalytic performance of Pt/3DOM-$Ce_{1-x}Bi_xO_{2-\delta}$ in the aerobic oxidation of 5-hydroxymethyl-2-furfural allows us to reveal the promoted catalytically active sites: the asymmetrical oxygen vacancies coordinated with one Bi and up to three Ce cations, such as Bi-□(-Ce)$_3$, where □ represents an oxygen vacancy, which can easily gain oxygen atoms in favor of the CeO_2 structure, and, when filled with oxygen, easily release oxygen anions in favor of six-coordination for Bi^{3+}. The loss of electrons in the reduction of oxygen atoms at these sites would be replenished by electron transfer from Pt nanoparticles, eventually promoting the oxidation potential of the Pt nanoparticles. The present work points out that the promoted catalytic properties in Bi-doped CeO_2 are mainly due to the asymmetric structures of the oxygen vacancies, rather than simply to the number of oxygen vacancies. The newly proposed model of asymmetrical active sites and electron transfer mechanism may shed light on the physicochemical properties of other solid solution substrate-supported metal nanoparticle catalysts.

© 2018 Elsevier Inc. All rights reserved.

1. Introduction

Supported metal nanocatalysts are commonly used in the chemical industry and have been investigated extensively. However, to identify the active sites and to understand electron transfer process in between the metal nanoparticles and the substrates are still challenging [1–3]. To evade the extreme difficulties of direct detection of the catalytically active sites and the charge transfer, we tried to gain the relevant information on changes in structures of catalysts and in catalytic activity of selected reactions, to reveal the active sites via an indirect method. The first selected example was Pt nanocatalyst supported by Bi-doped $CeO_{2-\delta}$ used for aerobic oxidation of 5-hydroxymethyl-2-furfural (HMF).

As far as practical catalysts are considered, CeO_2 and its ternary oxides, as efficient catalysts or catalyst carriers, have been widely used in many catalytic systems [4]. The low redox potential between Ce^{3+} and Ce^{4+} (1.3–1.8 V) and high oxygen storage capacity allow CeO_2–based catalysts to exhibit promising catalytic activity for aerobic oxidation of various reactants, such as CO [5,6], soot [7,8], and alcohols [9,10].

Biomass-derived HMF is considered an important intermediate from renewable biomass to industrial chemicals. It can be obtained from inexpensive and plentiful cellulosic derivatives, such as fructose, glucose, and cellulose [11–13], and can be converted to a series of important chemical compounds through aerobic oxidation, such as 2,5-diformylfuran (DFF), 5-hydroxymethyl-2-furancar boxylic acid (HMFCA), 5-formyl-2-furancarboxylic acid (FFCA), and 2,5-furandicarboxylic acid (FDCA) [14,15]. Especially, its oxidation product, FDCA, is one of the top value-added platform chemicals from biomass, and can be used as a monomer for the production of new polyesters and nylons [16]. Metal-oxide-supported noble-metal nanocatalysts are considered to be efficient and promising catalysts for the aerobic oxidation of HMF toward FDCA [17–19]. Among these, CeO_2-supported Au [20–22], Pt [23], or Au–Cu alloy [20] nanocatalysts exhibit notably enhanced catalytic performance in comparison with catalysts using other oxide carriers. Moreover, Bi-doped CeO_2, as an efficient carrier,

* Corresponding authors at: Institute of New Catalytic Materials Science and MOE Key Laboratory of Advanced Energy Materials Chemistry, School of Materials Science and Engineering, National Institute of Advanced Materials, Nankai University, Tianjin 300350, China.

E-mail addresses: lllou@nankai.edu.cn (L.-L. Lou), sxliu@nankai.edu.cn (S. Liu), wzhou@st-andrews.ac.uk (W. Zhou).

https://doi.org/10.1016/j.jcat.2018.06.025
0021-9517/© 2018 Elsevier Inc. All rights reserved.

can further improve their catalytic properties [21,23]. Although it is believed that the promotion of the catalytic properties using CeO_2 as a catalyst carrier is mainly attributable to a large number of oxygen vacancies on the surface of the oxides, giving a true composition of $CeO_{2-\delta}$, till now, our understanding of the role of oxygen vacancies and possible charge transfer in between the metal particles and the carriers has still been superficial.

In the present work, a series of three-dimensionally ordered macroporous (3DOM) $Ce_{1-x}Bi_xO_{2-\delta}$ were fabricated using polymethylmethacrylate (PMMA) colloidal crystals as a template and employed as catalyst carriers to support Pt nanoparticles. We found that the macroporous structure of these specimens could indeed greatly facilitate mass transfer. More importantly, significant promotion of electron transfer from Pt nanoparticles to Bi-doped $CeO_{2-\delta}$ and catalytic performance of these catalysts in the aerobic oxidation of HMF were observed in comparison with the Bi-free catalyst. We infer, based on the experimental data, that the asymmetrical vacancy sites, represented by Bi-□(-Ce)$_3$, where □ represents an oxygen vacancy, have different properties from the symmetrical vacancy sites, e.g., (Ce-)$_2$□(-Ce)$_2$ and (Bi-)$_2$□(-Bi)$_2$. The role of Bi-doping in the catalytic process is elucidated in a proposed mechanism, which may be used for explanation of many other nanoscale catalysts supported by metal oxides, where the interaction between the surface nanoparticles and the oxide support is significant.

2. Experimental

2.1. Materials

All chemicals were obtained from commercial sources and used without further purification. HMF (97%) and FDCA (98%) were purchased from Heowns Biochemical Technology Co. HMFCA (98%) was obtained from Matrix Scientific. DFF (98%) was provided by Sun Chemical Technology Co. FFCA (98%) was supplied by Toronto Research Chemicals. In quantitative analysis of chromatograms, the above specimens were used as the standards. Methanol, potassium persulfate (KPS, $K_2S_2O_8$), and sodium bicarbonate were obtained from Sinopharm Chemical Reagent Co. Polyvinylpyrrolidone (PVP, MW = 58,000) was obtained from Tianjing Guangfu Fine Chemistry Research Institute. Methyl methacrylate (MMA), ethylene glycol, ascorbic acid, cerium(III) nitrate hexahydrate ($Ce(NO_3)_3{\cdot}6H_2O$), bismuth(III) nitrate pentahydrate ($Bi(NO_3)_3{\cdot}5H_2O$), and chloroplatinic acid hexahydrate ($H_2PtCl_6{\cdot}6H_2O$) were purchased from Aladdin Chemicals Co.

2.2. Characterization methods

Powder X-ray diffraction (XRD) patterns were recorded on a Rigaku SmartLab 3 kW diffractometer with CuKα X-rays (λ = 1.541 Å) operating at 40 kV and 40 mA, in a 2θ range of 20–90° with a scanning rate of 6° min^{-1}. N_2 sorption analysis was carried out on a Micromeritics TriStar 3000 analyzer. The pore-size distribution was calculated according to the Barrett–Joyner–Halenda (BJH) method and the surface area was determined by the Brunauer–Emmett–Teller (BET) method. FEI Tecnai G2 F20 transmission electron microscopy (TEM) and JEOL JSM-7500F field-emission scanning electron microscopy (SEM) equipped with energy-dispersive X-ray spectrometry (EDS) were used to observe the morphological and structural features of the produced specimens. Inductively coupled plasma atomic emission spectrometry (ICP-AES) analysis was performed on an IRIS Intrepid II XSP instrument from Thermo Fisher Scientific. X-ray photoelectron spectrometry (XPS) characterization was carried out using a Kratos Axis Ultra DLD spectrometer employing a monochromatic Al*K*α X-ray source ($h\nu$ = 1486.6 eV), and the binding energy was corrected using the C1*s* peak (BE = 284.6 eV) of carbon contaminants as an internal standard. Raman spectra were collected on a Renishaw inVia model Raman microscope with a CCD detector (Renishaw, UK). The samples were excited using radiation at 514.5 nm. H_2 temperature-programmed reduction (H_2 TPR) and pulse CO chemisorption experiments were carried out on a Micromeritics ChemiSorb 2750 analyzer with a thermal conductivity detector. An Agilent 1200 series high-performance liquid chromatograph (HPLC) equipped with a Waters Atlantis T3 column and a UV–vis detector operating at 271 nm was used to analyze the reaction solution. A H_3PO_4 aqueous solution (1 mmol L^{-1}) was used as the mobile phase at a flow rate of 0.6 mL min^{-1}.

2.3. Synthesis of $Ce_{1-x}Bi_xO_{2-\delta}$ materials

$Ce_{1-x}Bi_xO_{2-\delta}$ materials with 3DOM structure were synthesized using a PMMA colloidal crystal (Fig. S1 in the Supplementary Material) as a template. The PMMA colloidal crystal templates, with an average diameter of ca. 300 nm, were synthesized through an emulsifier-free emulsion polymerization technique according to our previous work [24].

Supplementary data associated with this article can be found, in the online version, at https://doi.org/10.1016/j.jcat.2018.06.025.

In a typical synthesis process of 3DOM-$Ce_{1-x}Bi_xO_{2-\delta}$ materials, ethylene glycol (2 mL), methanol (7 mL), nitric acid (1 mL, 68 wt%), and ascorbic acid (10 mmol) were dissolved in deionized water (10 mL). $Ce(NO_3)_3{\cdot}6H_2O$ and $Bi(NO_3)_3{\cdot}5H_2O$ (with mole numbers $n_{Bi} + n_{Ce}$ = 10 mmol) with a selected ratio were added into this solution. After 3 h stirring at room temperature, a PMMA colloidal crystal (8.0 g) was soaked in the prepared solution for 3 h. Following a filtration and vacuum-drying process, the yellowish sample was calcined in an air flow (80 mL min^{-1}) at a ramp rate of 1 °C min^{-1} from room temperature to 550 °C and maintained at this temperature for 4 h to remove the template. 3DOM-$Ce_{1-x}Bi_xO_{2-\delta}$ (x = 0, 0.1, 0.2, 0.3) materials with different Bi^{3+} doping levels were obtained. For comparison, the nanosized $Ce_{1-x}Bi_xO_{2-\delta}$ samples were prepared using the same method, but in the absence of a PMMA colloidal crystal template. The obtained samples were designated as $Ce_{1-x}Bi_xO_{2-\delta}$ (x = 0, 0.1, 0.2, 0.3).

2.4. Synthesis of Pt/3DOM-$Ce_{1-x}Bi_xO_{2-\delta}$ catalysts

3DOM-$Ce_{1-x}BixO_{2-\delta}$ or $Ce_{1-x}Bi_xO_{2-\delta}$ (0.15 g) was dispersed in an aqueous solution of $H_2PtCl_6{\cdot}6H_2O$ (1.59 mL, 5.0 mg mL^{-1}) under stirring in an ultrasonic bath for 10 min, and the resulting mixture was continually stirred for another 5 h. An ethylene glycol solution of PVP (0.31 mmol in 40 mL) was then added into the mixture. After further stirring for 30 min, the reaction mixture was heated to 130 °C and aged for 4 h to ensure completion of the reaction. The product was centrifuged and washed several times with absolute ethanol and dried at 55 °C for 12 h. The obtained catalysts were designated as Pt/3DOM-$Ce_{1-x}Bi_xO_{2-\delta}$ and Pt/$Ce_{1-x}Bi_xO_{2-\delta}$, respectively. The nominal Pt content in these catalysts was 2 wt %, while the results of ICP-AES characterization indicated that the actual Pt loading was about 1.88 wt%.

2.5. Oxidation of HMF

The catalyst (0.039 g) was added into a solution of HMF (0.40 mmol) and $NaHCO_3$ (1.6 mmol) in deionized water (20 mL). The suspension was heated to 90 °C under stirring and bubbled with O_2 at a flow rate of 70 mL min^{-1}. An aliquot (50 μL) of the reaction mixture was taken out at given intervals and diluted to 5 mL with deionized water in a volumetric flask. The liquid sample was then syringe-filtered through a 0.2 μm PTFE membrane and

analyzed by HPLC. The concentrations of HMF, HMFCA, FFCA, and FDCA in the reaction solutions were measured by HPLC using the external standard calibration curve method. To evaluate the relative standard deviation (RSD) of the reaction results, four parallel experiments were carried out by using Pt/3DOM-$Ce_{0.8}Bi_{0.2}O_{2-\delta}$ as catalyst. The RSD values for yield of HMFCA, FFCA, and FDCA were determined as 1.7%, 2.4%, and 2.5%, respectively.

2.6. Computational methods

The DFT + U calculation using the Vienna ab initio simulation package (VASP) [25,26] was introduced to investigate the thermodynamic properties of obtained solid solution samples. All calculations in this work used the generalized gradient approximation (GGA-PW91) [27] as the exchange-correlation functional, and an energy cutoff of 500 eV was used for the plane-wave expansion of the electronic wave function. The DFT + U method evaluated the on-site Coulomb and exchange interactions in the localized 4*f* orbital electrons of Ce by adding an effective Hubbard *U* parameter to repulse electrons on the same orbitals [28,29]. It was reported that the theoretical *U* value was 5 eV [30,31]. $p(2\sqrt{3} \times 3)$ slab models of Ce(1 1 1) with the top four atomic layers relaxed and the bottom three layers fixed were used in the present work; the corresponding *k*-point meshes were set to 2 × 2 × 1. The vacuum space was set to 20 Å between the slabs to minimize their interaction.

3. Results and discussion

3.1. Characterization of 3DOM-$Ce_{1-x}Bi_xO_{2-\delta}$ specimens

Initial characterization of the 3DOM-$Ce_{1-x}Bi_xO_{2-\delta}$ samples was by XRD as shown in Fig. 1. All the diffraction peaks can be indexed onto a CeO_2-like unit cell, with a peak shift to a lower angle region corresponding to the Bi-doping, indicating a solid solution state in the whole compositional range up to the Bi-doping of 30%. This can be understood, since the high-temperature phase, δ-Bi_2O_3, also has a fluorite structure with 25% oxygen vacancies, which can be stabilized at room temperature in the form of a solid solution with fewer oxygen vacancies [32]. In addition, the wide peaks of these patterns indicate that the crystal sizes are quite small.

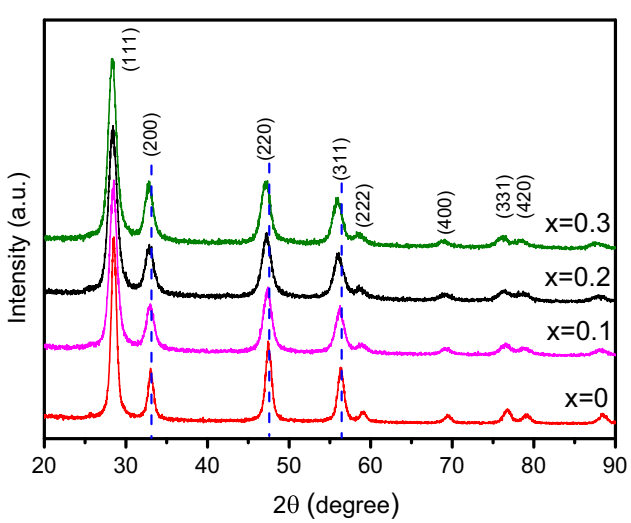

Fig. 1. XRD patterns of 3DOM-$Ce_{1-x}Bi_xO_{2-\delta}$ specimens with *x* from 0 to 0.3. The diffraction peaks are indexed to the CeO_2-like face-centered cubic unit cell with *a* = 0.5416 nm (JCPDS 34-0394). The dashed lines mark the peak positions of the *x* = 0 sample.

A typical SEM image of 3DOM-$Ce_{1-x}Bi_xO_{2-\delta}$ (*x* = 0.2) is shown in Fig. 2a. More SEM images of 3DOM-$Ce_{1-x}Bi_xO_{2-\delta}$ at lower magnifications are shown in Fig. S2. It can be seen from these images that a well-ordered array of cages, with an inverse opal structure, appears in the porous specimens. A typical diameter of the cages (negative replica of the close packed PMMA colloidal spheres) is about 160 nm, implying a shrinkage of ca. 47% in comparison with the size of PMMA spheres. The cages are interconnected via open windows about 78 nm in diameter, and the average thickness of cage walls is about 23 nm. EDS elemental mapping of 3DOM-$Ce_{0.8}Bi_{0.2}O_{2-\delta}$ exhibits even distributions of both Ce and Bi elements in this solid solution material, as shown in Fig. 2b.

The macroporous structure and specific surface areas of these 3DOM-$Ce_{1-x}Bi_xO_{2-\delta}$ materials were measured by the nitrogen sorption method. The type II characteristic isotherms with an H3 hysteresis loop in the relative pressure (p/p_0) range 0.8–1.0 were observed from 3DOM-$Ce_{1-x}Bi_xO_{2-\delta}$, indicating the existence of macroporous structure. The BET surface areas of the 3DOM-$Ce_{1-x}Bi_xO_{2-\delta}$ specimens are in the range 30–42 $m^2\ g^{-1}$ (Fig. S3 and Table S1).

Bi^{3+} cations have six-coordination of oxygen in the fluorite-type δ-Bi_2O_3, leaving two oxygen vacancies in the eight-coordinated environment. In the present work, Raman spectroscopy was used to detect any possible local distortion induced by such Bi-doping (Fig. 3). The spectrum of Bi-free CeO_2 displays a strong peak at 460 cm^{-1}, which is assigned to the F_{2g} vibrational mode of cubic fluorite structure of CeO_2 [33]. With the Bi^{3+}-doping, this peak slightly red shifts to a lower wavenumber, suggesting an obvious variation of the Ce-O bonding symmetry [34]. The peak at 517 cm^{-1}, being absent in pure CeO_2 and increasing in intensity with the Bi-doping, can be assigned to BiO_6 octahedral units in fluorite-type CeO_2 structure. This peak was also detected from fluorite-type δ-Bi_2O_3 [35,36]. The peak at 580 cm^{-1}, also absent in pure CeO_2, can be assigned to Ce^{3+}-O bonds associated with the asymmetric Bi^{3+}-□(-Ce^{3+})$_3$ sites [37]. The curve fitting of the Raman spectra (Fig. S4a–c) suggests that 3DOM-$Ce_{0.8}Bi_{0.2}O_{2-\delta}$ has the largest amount of Ce^{3+} among these specimens.

To further quantitatively determine the concentration of Ce^{3+}, which normally coexists with oxygen vacancies, Ce3*d* and O1*s* XPS spectra of these catalysts were measured. Ten characteristic peaks are observed in the Ce3d curves (Fig. 4a). The five peaks centered at 880.6, 882.2, 885.3, 888.8, and 898.0 eV, corresponding to v_0, v, v', v'', and v''', respectively, can be attributed to the Ce3$d_{5/2}$ contributions. The peaks at 899.2, 900.7, 904.0, 907.3, and 916.5 eV, corresponding to u_0, u, u', u'', and u''', respectively, are derived from the Ce3$d_{3/2}$ contributions. Among these Ce3*d* peaks, u_0, u' and v_0, v' can be ascribed to $Ce^{3+}3d_{3/2}$ and $Ce^{3+}3d_{5/2}$, while the peaks labeled as u, u'', u''' and v, v'', v''' are assigned to $Ce^{4+}3d_{3/2}$ and $Ce^{4+}3d_{5/2}$, respectively [38,39]. It can be seen that more Ce^{3+} species are detected in all the Bi-doped specimens than in the Bi-free CeO_2. 3DOM-$Ce_{0.8}Bi_{0.2}O_{2-\delta}$ exhibits the highest ratio of Ce^{3+} to total Ce (16.5%) among these specimens.

O1*s* XPS was employed to study the chemical states of oxygen in the surface regions of 3DOM-$Ce_{1-x}Bi_xO_{2-\delta}$. As shown in Fig. 4b, the peaks centered at 529.0–529.1 eV can be attributed to the lattice O^{2-} (denoted as O_β), and the peaks centered at 531.2–531.4 eV can be assigned to the chemisorbed oxygen species (denoted as O_α), such as O_2^{2-} and O_2^- [40]. The weak peaks at ~533 eV can be attributed to the absorbed water [41]. The ratio $O_\alpha/(O_\alpha + O_\beta)$ represents the oxygen activation capacity of the specimens, which is normally related to their number of oxygen vacancies. It can be found that 3DOM-$Ce_{0.8}Bi_{0.2}O_{2-\delta}$ exhibits the largest amount of O_α, which is well consistent with the results of Ce3*d* XPS.

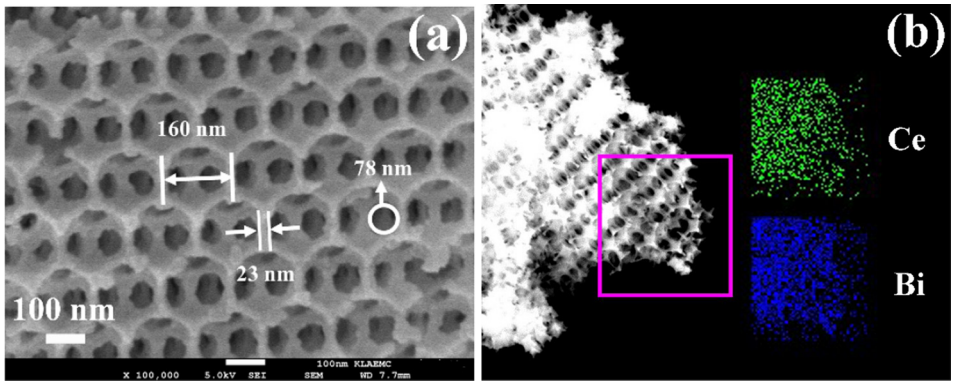

Fig. 2. (a) SEM image and (b) EDS elemental mapping of 3DOM-$Ce_{0.8}Bi_{0.2}O_{2-\delta}$. The dimensions of the cage, the intercage window, and the wall thickness are marked in (a).

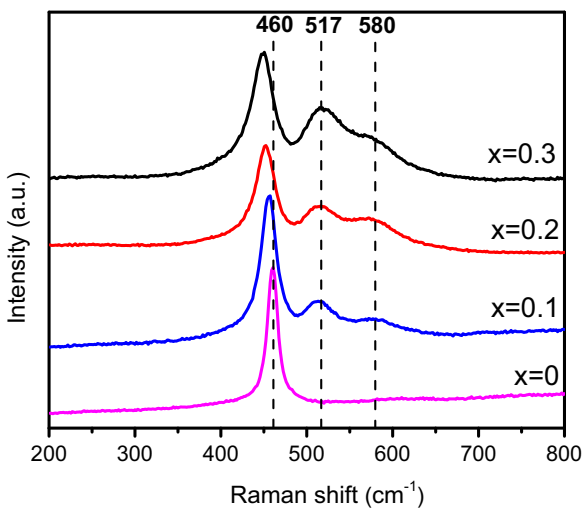

Fig. 3. Raman spectra of the 3DOM-$Ce_{1-x}Bi_xO_{2-\delta}$ specimens with x from 0 to 0.3.

3.2. Characterization of Pt/3DOM-$Ce_{1-x}Bi_xO_{2-\delta}$ catalysts

After deposition of Pt nanoparticles, the inverse opal morphology of the 3DOM-$Ce_{1-x}Bi_xO_{2-\delta}$ particles was unchanged, as seen in the TEM image of Pt/3DOM-$Ce_{0.8Bi0.2}O_{2-\delta}$ (Fig. S5). At a higher magnification, Pt nanocrystallites dispersed on the surface of the carrier are visible as dark spots in TEM images (Fig. 5a). The particle size distribution, measured for 130 randomly chosen Pt nanoparticles, is quite narrow, with an average diameter of about 2.1 nm. The HRTEM image of Pt/3DOM-$Ce_{0.8Bi0.2}O_{2-\delta}$ catalyst in Fig. 5b shows lattice fringes corresponding to the (1 1 1) planes of cubic CeO_2 and Pt crystals. The oxide wall is polycrystalline, constructed with Bi-doped CeO_2 nanocrystals, which is consistent with the observation of the wide XRD peaks. The XRD patterns of these Pt/3DOM-$Ce_{1-x}Bi_xO_{2-\delta}$ catalysts are shown in Fig. S6. All the diffraction peaks derived from a CeO_2-like face-centered cubic unit cell were still distinct after the deposition of Pt nanoparticles. No diffraction peaks derived from Pt particles can be observed because of their nanoscale particle sizes.

The obtained Pt/3DOM-$Ce_{1-x}Bi_xO_{2-\delta}$ catalysts were investigated by XPS to reveal electron transfer from Pt to carrier. As seen

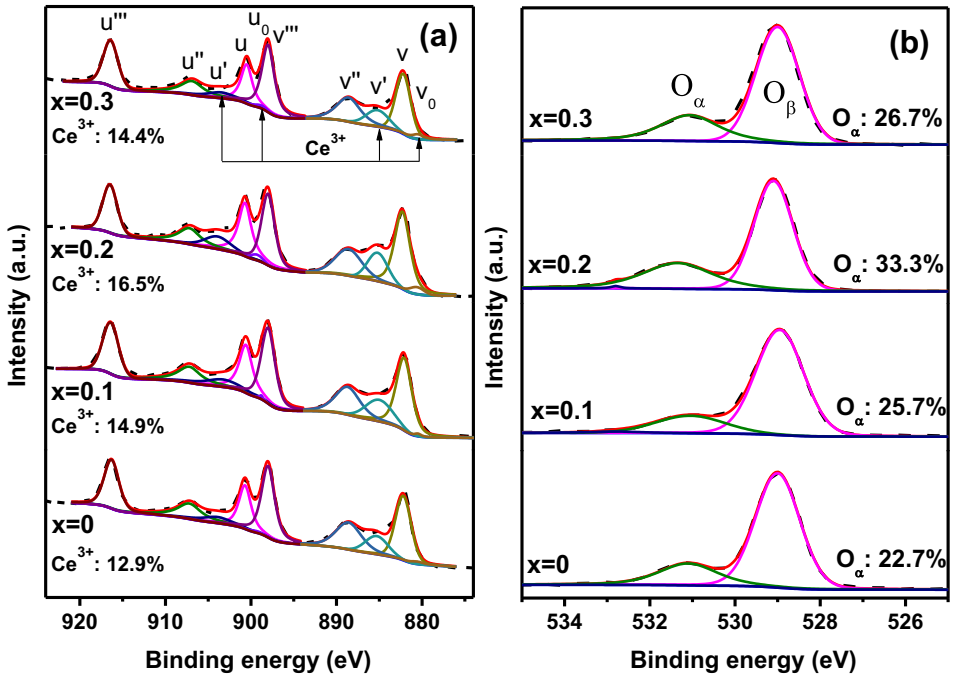

Fig. 4. (a) Ce3d and (b) O1s XPS spectra of 3DOM-$Ce_{1-x}Bi_xO_{2-\delta}$ with x from 0 to 0.3.

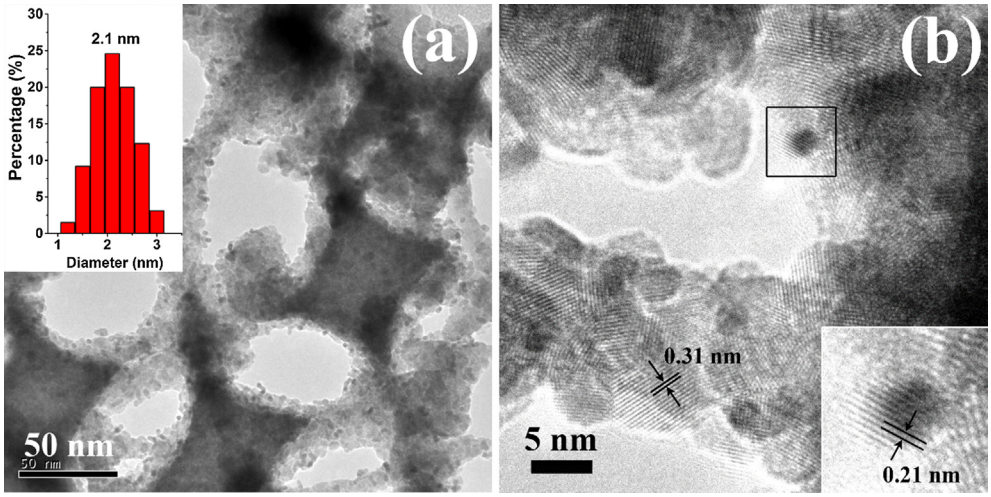

Fig. 5. (a) TEM and (b) HRTEM images of Pt/3DOM-$Ce_{0.8}Bi_{0.2}O_{2-\delta}$ catalyst. The inset in (a) is the Pt particle size distribution and the inset in (b) is an enlarged image of the Pt particle marked by a square. The measured *d*-spacings of 0.21 and 0.31 nm correspond to the (1 1 1) planes in Pt and 3DOM-$Ce_{0.8}Bi_{0.2}O_{2-\delta}$, respectively.

in Fig. 6a, the proportion of Ce^{3+} in Pt/3DOM-$Ce_{1-x}Bi_xO_{2-\delta}$ increases significantly from that in 3DOM-$Ce_{1-x}Bi_xO_{2-\delta}$, which means that the Ce^{4+} ions are further reduced to Ce^{3+} with the deposition of Pt. Fig. 6b shows the Pt4*f* spectra from Pt/3DOM-$Ce_{1-x}Bi_xO_{2-\delta}$. The deconvoluted peaks with binding energies of 70.6–70.7 and 73.9–74.0 eV can be attributed to Pt4$f_{7/2}$ and Pt4$f_{5/2}$ of Pt^0, respectively. The peaks assigned to Pt^{2+} appear at 71.8 and 75.2 eV. It can be observed that Pt mainly exists as Pt^0 in these samples. But about 26.9–34.3% of Pt are oxidized to Pt^{2+}. Taking into account the further reduction of Ce^{4+} and the partial oxidation of Pt in Pt/3DOM-$Ce_{1-x}Bi_xO_{2-\delta}$ catalysts, the charge transfer from Pt to 3DOM-$Ce_{1-x}Bi_xO_{2-\delta}$ can be confirmed. In addition, from the Bi4*f* XPS spectra of 3DOM-$Ce_{0.8Bi0.2}O_{2-\delta}$ and Pt/3DOM-$Ce_{0.8}Bi_{0.2}O_{2-\delta}$ (Fig. S7), it can be seen that the Bi cations are in the Bi^{3+} state.

The percentages of Ce^{3+} in 3DOM-$Ce_{1-x}Bi_xO_{2-\delta}$ before and after the deposition of Pt and the relative abundances of Pt^{2+} in Pt/3DOM-$Ce_{1-x}Bi_xO_{2-\delta}$ catalysts are listed in Table 1. It is interesting to see that Pt/3DOM-$Ce_{0.8}Bi_{0.2}O_{2-\delta}$, with the largest amount of Pt^{2+}, exhibits the largest extra increase of Ce^{3+} induced by the deposition of Pt, suggesting the largest amount of charge transfer from Pt to carrier, in spite of the largest amount of Ce^{3+} also existing in this catalyst. This observation is of great interest, since we normally think that the existence of Ce^{3+} would imply that charge transfer from Pt to carrier is inhibited [1,42].

3.3. Effect of Bi-doping on structural properties

The appearance of the maximum concentrations of Ce^{3+} and Pt^{2+} cations in the 20% Bi-doped sample indicates that the doping effect on the electronic structure of CeO_2 is not monotonic. Although there are several differently coordinated oxygen sites on the crystal surface, such as M–O–M, M–O–M_2, and M_2–O–M_2 (M = Ce or Bi), to simplify the discussion, we only use the four-coordinated oxygen

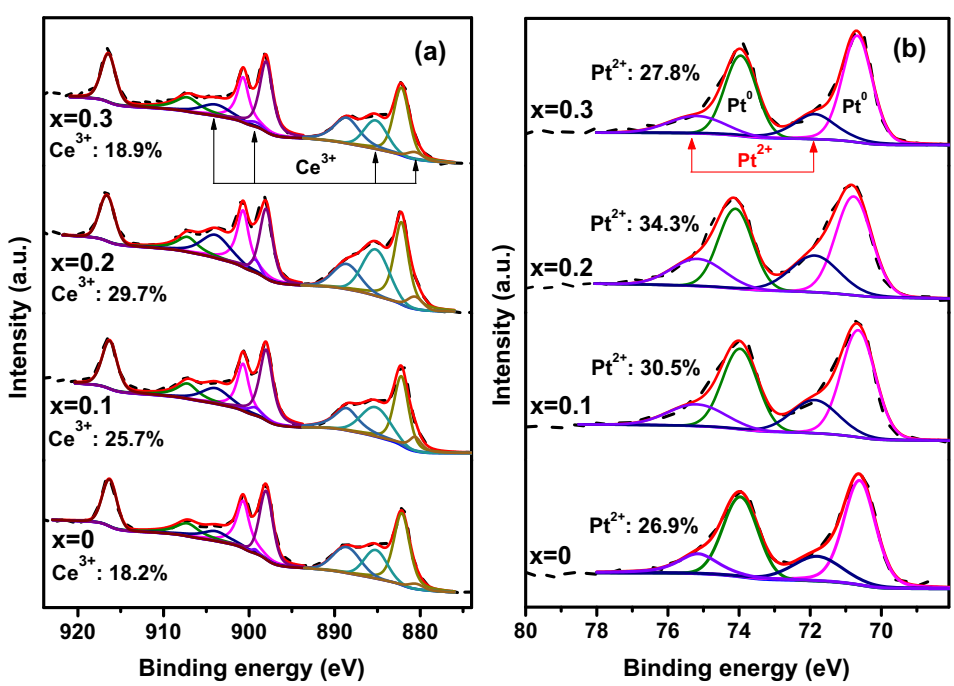

Fig. 6. (a) Ce3*d* and (b) Pt4*f* XPS spectra of Pt/3DOM-$Ce_{1-x}Bi_xO_{2-\delta}$, with *x* from 0 to 0.3.

Table 1
The concentrations (%) of Ce^{3+} and Pt^{2+} cations in the surface regions of 3DOM-$Ce_{1-x}Bi_xO_{2-\delta}$ and Pt/3DOM-$Ce_{1-x}Bi_xO_{2-\delta}$ detected by XPS (A) before and (B) after deposition of Pt.

Sample	Ce^{3+}/Ce (%)		Pt^{2+}/Pt (%)
	(A)	(B)	
3DOM-CeO_2	12.9	18.2	26.9
3DOM-$Ce_{0.9Bi0.1}O_{2-\delta}$	14.9	25.7	30.5
3DOM-$Ce_{0.8}Bi_{0.2}O_{2-\delta}$	16.5	29.7	34.3
3DOM-$Ce_{0.7}Bi_{0.3}O_{2-\delta}$	14.4	18.9	27.8

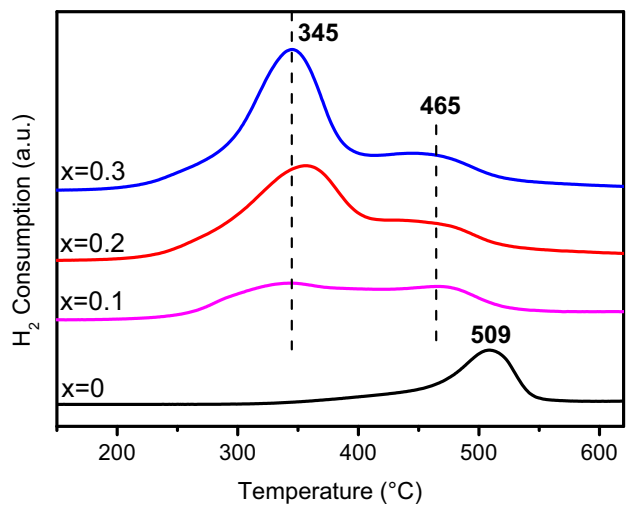

Fig. 7. The H_2 TPR results of the 3DOM-$Ce_{1-x}Bi_xO_{2-\delta}$ specimens, with x from 0 to 0.3.

sites as an example in our elucidation of the Bi-doping effect. When an octacoordinated Ce^{4+} is replaced by a hexacoordinated Bi^{3+}, two oxygen vacancies will be generated around this Bi^{3+}, forming a cluster of (Ce-)$_3$□-Bi-□(-Ce)$_3$, as shown in Fig. S8a. Around the oxygen vacancy, Bi^{3+} maintains its original oxidation state and Ce^{4+} is reduced to Ce^{3+}, forming a cluster of Bi^{3+}-□(-Ce^{3+})$_3$. The actual oxidation state of a cerium cation depends on its total coordination number of oxygen. It is obvious that the concentration of Ce^{3+} would be increased with the Bi-doping until formation of stable Bi-□-Bi or tetrahedral (Bi-)$_2$□(-Bi)$_2$ clusters.

When the Bi-doping level is low, all the Bi^{3+} cations are separated by Ce. In other words, no Bi-O-Bi or Bi-□-Bi connection forms. The shortest possible distance between two Bi cations is the same as the fluorite unit cell parameter. The theoretical maximum Bi substitution in such a structure is 25%, according to the ordered model shown in Fig. S8b. In the range of Bi-doping below 25%, including $Ce_{0.9}Bi_{0.1}O_{2-\delta}$ and $Ce_{0.8}Bi_{0.2}O_{2-\delta}$, part of the Bi^{3+} cations replace six-coordinated Ce^{3+} without breaking the neutrality and the rest of the Bi^{3+} cations replace eight-coordinated Ce^{4+} plus two associated O^{2-}, breaking the local charge balance. To meet the requirement of neutrality at the Bi-□(-Ce)$_3$ sites, some Ce^{4+} will be reduced to Ce^{3+}. Consequently, with Bi-doping, not only the number of oxygen vacancies, but also the number of Ce^{3+} would increase.

When the content of Bi^{3+} is further increased to 30%, two or more Bi^{3+} would link to the same oxygen vacancy, forming Bi-□-Bi and even larger Bi-rich clusters. This so-called "like with like" phenomenon has been often found in fluorite-type solid solutions [43]. The number of asymmetrical Bi-□(-Ce)$_3$ sites would decrease, while a decrease of the concentration of holes in the Pt nanoparticles would be observed.

Compared with the symmetrical (Ce-)$_2$□(-Ce)$_2$ sites, the asymmetrical Bi-□(-Ce)$_3$ sites would easily gain oxygen atoms to form Bi-O(-Ce)$_3$, and easily release oxygen anions to return to Bi-□(-Ce)$_3$. Simultaneously, the sites would receive electrons from Pt to replenish the lost electrons during the reduction of oxygen. Therefore, Pt/3DOM-$Ce_{0.8}Bi_{0.2}O_{2-\delta}$, with the largest number of Bi-□(-Ce)$_3$ sites, exhibits the greatest ability for electron transfer from Pt.

The difference between the oxygen sites in Bi-doped CeO_2, e.g., Bi-□(-Ce)$_3$ and the sites in pure CeO_2, e.g., (Ce-)$_2$□(-Ce)$_2$ can be experimentally confirmed by H_2-TPR of 3DOM-$Ce_{1-x}Bi_xO_{2-\delta}$, as shown in Fig. 7. With Bi^{3+}-doping, the reduction peaks of 3DOM-$Ce_{1-x}Bi_xO_{2-\delta}$ are shifted from 509 °C to at least two lower-temperature regions centered at ca. (I) 345 and (II) 465 °C, indicating the formation of new types of redox sites and the interaction between CeO_2 and the dopant ions. The reduction peaks located at 345 °C should be attributed to oxygen removal from the redox sites associated with Bi^{3+}, including Bi-O(-Ce)$_3$ clusters. The reduction peaks centered at 465 °C can be derived from the redox sites associated with Ce^{4+}, which moved from 509 °C to lower-temperature region because of the interaction between Ce^{4+} and the doped Bi^{3+} ions. The related hydrogen consumption data have been listed in Table S2. The results show unambiguously that Bi-doping not only decreases the reduction temperature, but also increases the H_2 consumption in comparison with pure CeO_2, suggesting better redox properties.

3.4. DFT calculation of the asymmetrical oxygen vacancy sites

To further prove the excellent oxygen adsorption ability and oxygen release ability of these asymmetrical Bi-□(-Ce)$_3$ sites compared with symmetrical (Ce-)$_2$□(-Ce)$_2$ sites, the adsorption energy of oxygen (E_{ads}) and the formation energy of oxygen vacancies [E_f(Ov)] of these sites were calculated. On the surface of CeO_2(1 1 1), the coordination number of oxygen in these oxygen vacancy sites is 3. Thus, Bi-□(-Ce)$_2$ and Ce-□(-Ce)$_2$ should be the main forms of these oxygen vacancy sites.

The E_{ads} of these sites was calculated as $E_{ads} = E_{A/S} - (E_A + E_S)$, where E_A, E_S, and $E_{A/S}$ represent the energy of adsorbed species, the energy of free substrate, and the total energy of the adsorbate–substrate system, respectively. The geometrical structures of O_2 adsorbed into asymmetrical Bi-□(-Ce)$_2$ or symmetrical Ce-□(-Ce)$_2$ sites are shown in Fig. 8a; the related E_{ads} data are listed in Table 2. The O_2 molecule was adsorbed at the hollow site of Bi-□(-Ce)$_2$ or Ce-□(-Ce)$_2$. It can be found that the adsorption of O_2 on these oxygen vacancy sites is an exothermic process. Although a lower E_{ads} of O_2 on the Ce-□-(Ce)$_2$ sites is obtained, the E_{ads} of O_2 on the Bi-□-(Ce)$_2$ sites is also very low (−4.61 eV), indicating that O_2 is easily adsorbed onto both oxygen vacancy sites. On the other hand, the bond length of adsorbed oxygen molecules on the Bi-O-(Ce)$_2$ sites is relatively shorter and the Bi-O and Ce-O bond lengths are significantly longer than those in the Ce-O-(Ce)$_2$ sites, as seen in Fig. 8a. This implies that the oxygen molecules on the Bi-O-(Ce)$_2$ sites are less stable and tend to leave as activated pieces. The charge imbalance at the Bi cations introduced by an extra Bi-O bond further increases the instability of the oxygen.

The E_f(Ov) of these sites (Fig. 8b) was calculated through the formula $E_f(\mathrm{Ov}) = E_{def} - E_{free} + \frac{1}{2}E_{O2}$, in which E_{def}, E_{free}, and E_{O2} are the energies of the defective structure with an oxygen vacancy, the perfect system, and the free molecular oxygen, respectively [44]. The obtained E_f(Ov) results are also listed in Table 2. The E_f(Ov) of the Ce-O(-Ce)$_2$ site is 1.67 eV, which is significantly higher than that of the asymmetrical Bi-O(-Ce)$_2$ site (0.70 eV). This result indicates that the oxygen atoms in the asymmetrical Bi-O(-Ce)$_2$

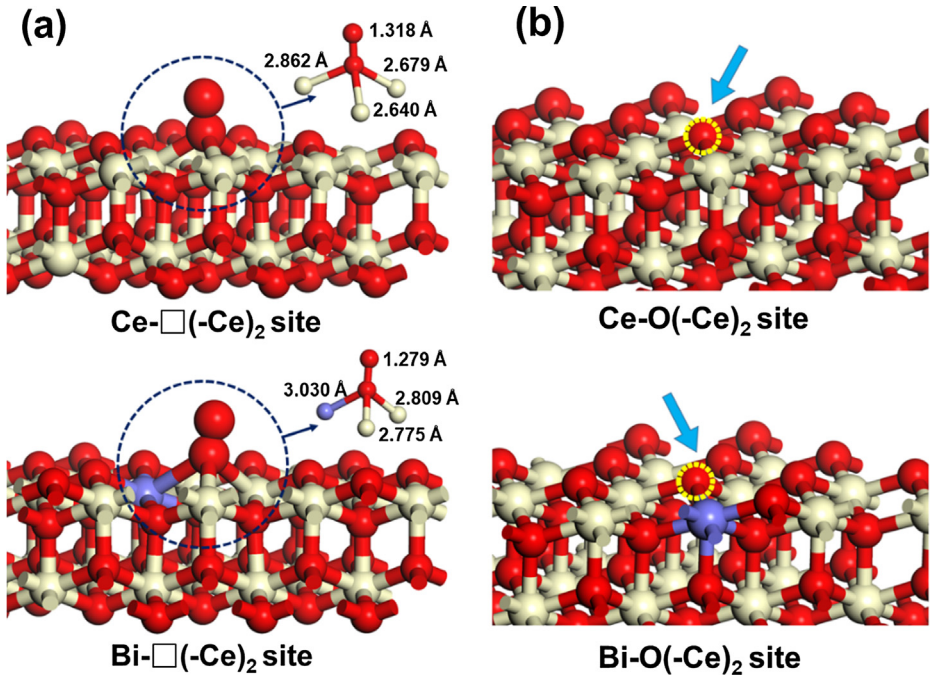

Fig. 8. (a) The geometries of O_2 adsorbed onto Bi-□(-Ce)$_2$ and Ce-□(-Ce)$_2$ sites. The relevant bond lengths are marked. (b) DFT-calculated structure for E_f(Ov) on Bi-O(-Ce)$_2$ and Ce-O(-Ce)$_2$ sites. The Ce^{4+}, O, Bi are colored gray, red. and purple, respectively. The circled O atoms in (b) are the oxygen to be released.

Table 2
The calculated adsorption energy of oxygen and the formation energy of oxygen vacancies on different sites of the CeO_2(1 1 1) surface.

Energy(eV)	Bi-□(-Ce)$_2$	Ce-□(-Ce)$_2$
E_{ads}	−4.61	−6.83
E_f(Ov)	0.70	1.67

sites are more active and easily released from these sites. The DFT calculation results further prove the notably enhanced redox property of these asymmetrical oxygen vacancy sites compared with symmetrical sites in pure $CeO_{2-\delta}$.

3.5. Effect of Bi-doping on catalytic performance

The influence of Bi-doping in Pt/3DOM-$Ce_{1-x}Bi_xO_{2-\delta}$ on catalytic performance was evaluated in the aerobic oxidation of HMF to FDCA at ambient pressure (Fig. 9). The final results after 10 h reaction over these catalysts and the calculated turnover frequency (TOF) values are listed in Table 3.

As shown in Fig. 9 and Table 3, all of these Pt/3DOM-$Ce_{1-x}Bi_xO_{2-\delta}$ catalysts exhibited good catalytic activity for the aerobic oxidation of HMF. In the first 2 h, FFCA was the main intermediate product in these reaction systems, indicating that the conversion from FFCA to FDCA is the rate-determining step of the reaction over Pt/3DOM-Ce1-x$Bi_xO_{2-\delta}$, which can be clearly observed from the kinetic simulation results according to the reported methods [46,47] based on these reaction data (as shown in Fig. S9), and was also found in relevant literature on Pt-based catalysts [19,48,49]. It is very different with Au- or Pd-catalyzed reactions [17,18,20–22,45], in which the dehydrogenation of the hydroxymethyl group of HMFCA to FFCA is the rate-determining step. Among these Pt/3DOM-$Ce_{1-x}Bi_xO_{2-\delta}$ catalysts, Pt/3DOM-CeO_2 exhibited relatively poor catalytic performance. When 10% of cerium were replaced with Bi^{3+}, the catalytic behavior of the catalyst was enhanced significantly. The highest yield of FDCA was achieved with 20% Bi-doping. When the Bi-doping level increased

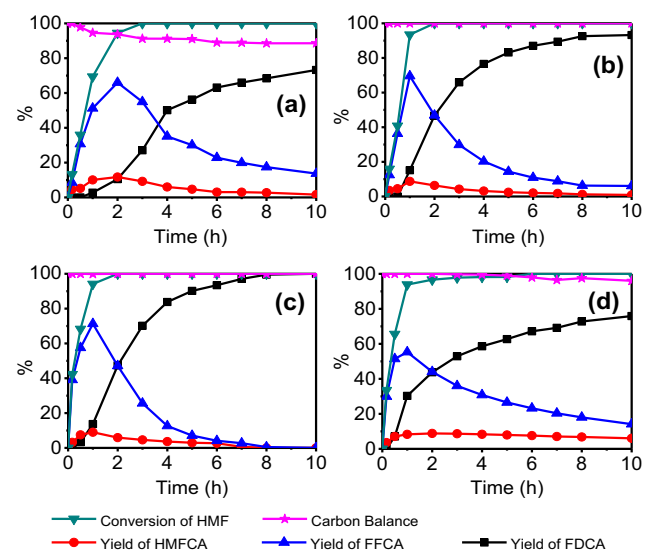

Fig. 9. Reaction profiles for the oxidation of HMF on Pt/3DOM-$Ce_{1-x}Bi_xO_{2-\delta}$ catalysts when (a) x = 0, (b) x = 0.1, (c) x = 0.2, and (d) x = 0.3. Reaction conditions: n_{HMF}/n_{Pt} = 100, n_{HMF}/n_{NaHCO3} = 0.25, 90 °C, with O_2 bubbling (70 mL min^{-1}).

to 30%, the yield of FDCA decreased to 76%. When the Bi-doping level increased further to 50%, the obtained Pt/3DOM-$Ce_{0.5Bi0.5}O_{2-\delta}$ catalyst exhibited the lowest yield of FDCA among these Pt/3DOM-$Ce_{1-x}Bi_xO_{2-\delta}$ catalysts (entry 5, Table 3). In addition, as shown in Table 3, the carbon balance values for the reactions over Pt/3DOM-$Ce_{0.9}Bi_{0.1}O_{2-\delta}$ and Pt/3DOM-$Ce_{0.8}Bi_{0.2}O_{2-\delta}$ (>99%) are notably higher than those over Pt/3DOM-$Ce_{0.7}Bi_{0.3}O_{2-\delta}$ (96%), Pt/3DOM-CeO_2 (89%), and Pt/3DOM-$Ce_{0.5}Bi_{0.5}O_{2-\delta}$ (85%), which can be attributed to the faster conversion of intermediate products to relatively stable FDCA over Pt/3DOM-$Ce_{0.9}Bi_{0.1}O_{2-\delta}$ and Pt/3DOM-$Ce_{0.8}Bi_{0.2}O_{2-\delta}$. It can be also observed from Table 3 that the TOF value of Pt/3DOM-$Ce_{0.8}Bi_{0.2}O_{2-\delta}$ reaches 9.27 min^{-1}, which is 2.9 times as high as that of Pt/3DOM-CeO_2. Compared

Table 3
Catalytic performance of Pt/3DOM-$Ce_{1-x}Bi_xO_{2-\delta}$ catalysts for the aerobic oxidation of HMF.[a]

Entry	Catalyst	HMF conv. (%)	Yield (%)			Carbon balance (%)	TOF value (min^{-1})[b]
			FDCA	FFCA	HMFCA		
1	Pt/3DOM-CeO_2	100	73	14	2	89	3.24
2	Pt/3DOM-$Ce_{0.9}Bi_{0.1}O_{2-\delta}$	100	93	6	1	>99	4.24
3	Pt/3DOM-$Ce_{0.8}Bi_{0.2}O_{2-\delta}$	100	>99	0	0	>99	9.27
4	Pt/3DOM-$Ce_{0.7}Bi_{0.3}O_{2-\delta}$	100	76	14	6	96	7.00
5	Pt/3DOM-$Ce_{0.5}Bi_{0.5}O_{2-\delta}$	100	66	14	5	85	–
6	3DOM-CeO_2	40	0	0	2	62	–
7	3DOM-$Ce_{0.8}Bi_{0.2}O_{2-\delta}$	50	4	3	2	59	–

[a] Reaction conditions: n_{HMF}/n_{Pt} = 100, n_{HMF}/n_{NaHCO3} = 0.25, 90 °C, 10 h, O_2 bubbling (70 mL min^{-1}).
[b] TOF values were calculated from the results at 10 min reaction using the equation [45,46] and Pt dispersion was determined by CO chemisorption: $TOF(min^{-1}) = \frac{Conv_{HMF}(\%)\times(n_{HMF}/n_{Pt})}{time(min)\times Ptdispersion}$.

with reported catalysts as listed in Table S3, Pt/3DOM-$Ce_{0.8}Bi_{0.2}O_{2-\delta}$ should be a promising catalyst under mild reaction conditions. Although the same optimized doping level of Bi^{3+} was found in Pt/3DOM-$Ce_{1-x}Bi_xO_{2-\delta}$ catalysts compared with the reported literature [21,23], an obviously different promoting mechanism of Pt/3DOM-$Ce_{1-x}Bi_xO_{2-\delta}$ compared with Pt/3DOM-CeO_2 was proposed in this work. We believe this Bi-doping effect is closely associated with the newly created asymmetrical oxygen vacancy site of Bi-□(-Ce)$_3$, as discussed above.

3.6. Role of the asymmetrical oxygen vacancy site in promoting electron transfer and catalytic performance

To investigate the electronic interaction between the sites of oxygen vacancy and the Pt nanoparticles, a calculation model with a tetrahedral Pt4 cluster adsorbed onto Bi-□(-Ce)$_2$, Ce-□(-Ce)$_2$, and Ce-O(-Ce)$_2$ sites on the surface of CeO_2(1 1 1), as described in Fig. 10, was employed. The Bader charge analysis was carried out to study the electron density of the Pt4 cluster [50,51], and the results are listed in Table 4. The Bader valence of Pt atoms adsorbed on Ce-based metal oxide can indicate the directional and the quantity of electron transfer [52]. It can be seen that the Bader valence of Pt atoms on Bi-□(-Ce)$_2$, Ce-□(-Ce)$_2$, and Ce-O(-Ce)$_2$ decreased by −0.71|e|, −0.62|e|, and −0.76|e|, respectively. The electropositivity of the Pt4 cluster indicates electron transfer from the Pt4 cluster to the carrier, which is consistent with the results of XPS characterization. Moreover, compared with the symmetrical Ce-□(-Ce)$_2$ sites, the Pt4 cluster adsorbed onto

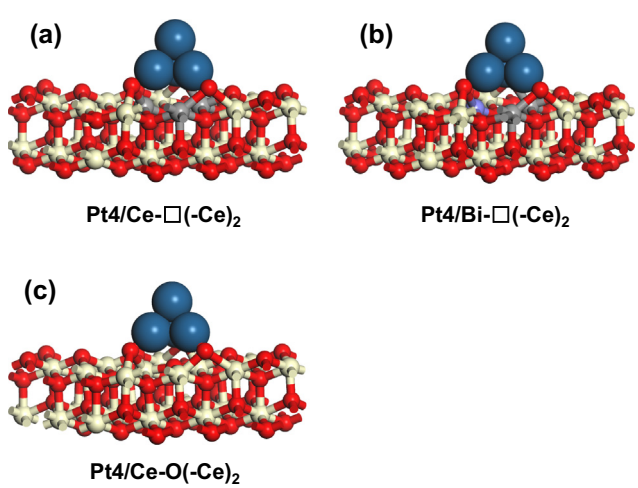

Fig. 10. Geometries of (a) Pt4/Ce-□(-Ce)$_2$, (b) Pt4/Bi-□(-Ce)$_2$, and (c) Pt4/Ce-O(-Ce)$_2$.

Table 4
The Bader charge and adsorption energy of the Pt4 cluster on Bi-□(-Ce)$_2$, Ce-□(-Ce)$_2$, or Ce-O(-Ce)$_2$ sites of theCeO_2(1 1 1) surface.

	Pt4/Bi-□(-Ce)$_2$	Pt4/Ce-□(-Ce)$_2$	Pt4/Ce-O(-Ce)$_2$
Bader valence |e|	−0.71	−0.62	−0.76
E_{ad} (eV)	−7.15	−7.67	−4.92

asymmetrical Bi-□(-Ce)$_2$ sites exhibited a larger amount of electron transfer, although from Bader charge analysis the strongest charge transfer took place on Pt4/Ce-O(-Ce)$_2$ sites.

To determine the preferred adsorption site of the Pt4 cluster on the surface of CeO_2(1 1 1), the adsorption energies are calculated and the results are listed in Table 4. The more negative adsorption energies of Pt4 adsorbed onto oxygen vacancy sites compared with Ce-O(-Ce)$_2$ sites indicates that Pt nanoparticles are likely to be preferentially adsorbed onto oxygen vacancy sites. From the results of DFT calculation, the existence of asymmetrical Bi-□(-Ce)$_3$ oxygen vacancy sites can effectively stabilize Pt nanoparticles and promote electron transfer from Pt to carrier.

However, the dehydrogenation reactions of HMF on the surfaces of Pt nanoparticles with the assistance of OH^- anions would leave excess electrons on Pt nanoparticles [53,54]. Therefore, a continuous electron transfer from Pt to carrier may exist on these Pt/3DOM-$Ce_{1-x}Bi_xO_{2-\delta}$ catalysts under aerobic oxidation conditions. It has been known that the oxygen vacancies in CeO_2-based materials can be active sites for oxygen activation. The adsorbed O_2 can be activated and converted to superoxo- or peroxo- oxygen (i.e., O_2^- or O_2^{2-}) as described in the equations

$$O_2 + Ce^{3+} \rightarrow O_2^- + Ce^{4+} \quad (1)$$

$$Ce^{4+} + e^- \rightarrow Ce^{3+} \quad (2)$$

$$O_2^- + e^- \rightarrow O_2^{2-}. \quad (3)$$

The O_2^{2-} can be dissociated to monatomic O^- and further reduced to lattice oxygen (O^{2-}) at these sites [55]. On the other hand, these active oxygen species can leave the crystals, restoring the oxygen vacancies, by reacting with H_2O to form H_2O_2 and OH^-:

$$O_2^{2-} + 2H_2O \rightarrow H_2O_2 + 2OH^-. \quad (4)$$

These O_2 activation reactions at the CeO_2 surface can consume a large number of electrons. Consequently, this process should be the real driving force of continuous electron transfer from Pt to carrier.

Following the above discussions, we are now able to propose a mechanism of Bi-doping promoting electron transfer and catalytic performance for the aerobic oxidation of HMF, as illustrated in Fig. 11. In this schematic, only tetrahedral clusters, Bi-O(-Ce)$_3$,

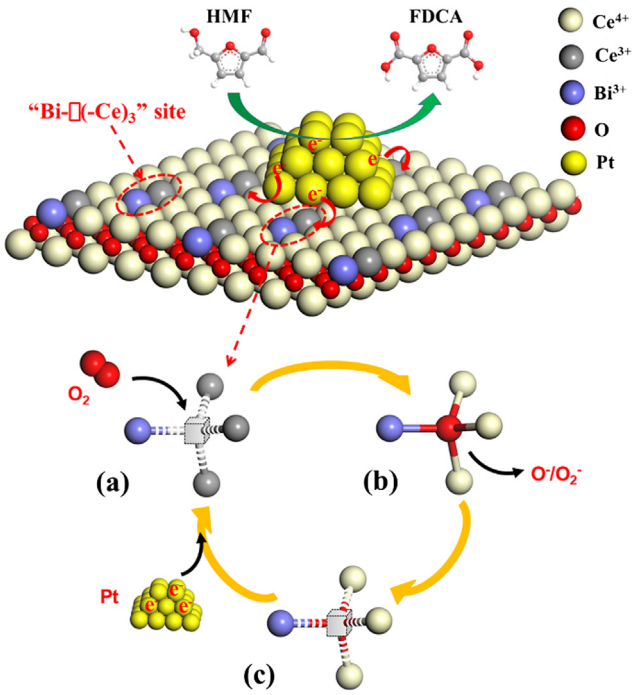

Fig. 11. Top: Plausible reaction mechanism of HMF oxidation over Pt/3DOM-$Ce_{1-x}Bi_xO_{2-\delta}$ catalysts. Surface oxygen anions are not shown for simplicity. Bottom: A schematic drawing to show a process of oxygen activation at a site of Bi-□(-Ce)$_3$.

were used to elucidate their role in the catalytic reaction, although they can be three- or two-coordinated on the crystal surface.

The principal role of Bi-doping in the improvement of catalytic activity is to modify the properties of the oxygen vacancies, allowing oxygen easy come, easy go. When the oxygen is removed, the Bi-□(-Ce)$_3$ cluster has a special electronic structure and an interesting improved redox property. Let us start with Bi^{3+}-□(-Ce^{3+})$_3$ (Fig. 11a). The vacancy is favorable to Bi^{3+} as far as the coordination number is considered, but not to cerium cations, which prefer eight-coordination. Therefore, it is still easy to adsorb oxygen. The adsorbed oxygen gains electrons from Ce^{3+} cations, forming a cluster of Bi^{3+}-O(-Ce^{4+})$_3$ (Fig. 11b).

The occupation of the vacancy favors Ce^{4+}, but generates too high a coordination number for Bi^{3+}, and an unbalanced charge at Bi^{3+}. The oxygen intends to leave as an anion, reacting with H_2O, leading to the formation of a Bi^{3+}-□(-Ce^{4+})$_3$ cluster (Fig. 11c). At this stage, electrons may transfer from the Pt nanoparticles to reduce the Ce^{4+} cations to stabilize the cluster, returning to Bi^{3+}-□(-Ce^{3+})$_3$. This three-step circle demonstrates how the oxygen vacancies activate oxygen from the solution and how a potential for electron transfer from Pt to the clusters is created.

On the other hand, 3DOM-CeO_2 and 3DOM-$Ce_{0.8}Bi_{0.2}O_{2-\delta}$ in the absence of Pt nanoparticles exhibit much lower catalytic performance for HMF oxidation, as listed in Table 3 (entries 6 and 7). About 40–50% of HMF are converted to side products through ketonization and condensation reactions [17,56]. This can be understood to mean that the Bi^{3+}-O(-Ce^{4+})$_3$ clusters cannot be self-reduced to Bi^{3+}-O(-Ce^{3+})$_3$ without receiving electrons from other parts of the particle. Therefore, the aerobic oxidation of HMF must occur on the Pt nanoparticles, leaving electrons there. The electrons are then donated to the Bi^{3+}-O(-Ce^{4+})$_3$ clusters in the carrier. The clusters unambiguously play an important role in synergistically promoting the reaction. The hole-rich Pt nanoparticles have the potential to attract OH^- anions and HMF molecules, resulting in the continuous oxidation of HMF to FDCA through dehydrogenation reactions on the surfaces of Pt nanoparticles. A more detailed process of the reactions is depicted in Scheme 1.

3.7. Effect of 3DOM structure

To investigate the influence of 3DOM structure on the catalytic performance of these catalysts, the nanosized Pt/$Ce_{1-x}Bi_xO_{2-\delta}$ catalysts were also evaluated in the oxidation of HMF under the same reaction conditions. The reaction results are shown in Fig. S10. It can be found from Figs. 9 and S10 that the Pt/3DOM-$Ce_{1-x}Bi_xO_{2-\delta}$ catalysts exhibit notably improved catalytic performance in the oxidation of HMF in comparison with Pt/$Ce_{1-x}Bi_xO_{2-\delta}$. Especially for the yield of FDCA, the 3DOM samples show significantly higher selectivity than the nonporous samples when the Bi-doping levels are the same. For instance, as seen in Figs. 9c and S10c, although comparable HMF conversions were obtained over Pt/3DOM-$Ce_{0.8Bi0.2}O_{2-\delta}$ and Pt/$Ce_{0.8}Bi_{0.2}O_{2-\delta}$ catalysts, an obviously increased FDCA yield over 10 h was achieved by the former (100%) in comparison with the latter (78%). The improved FDCA yield can be attributed to the 3DOM structure of these catalysts. First, the surface of the ordered macroporous structure may contain more defects created during the calcination to decompose PMMA, and become more suitable to house active Pt nanoparticles. Second, the interconnected and ordered macroporous structure can significantly facilitate the mass transfer of the reactants and products and therefore can promote the multistep oxidation of HMF.

3.8. Reusability of the catalyst

The stability of the Pt/3DOM-$Ce_{1-x}Bi_xO_{2-\delta}$ catalysts in the aerobic oxidation of HMF was investigated using Pt/3DOM-$Ce_{0.8}Bi_{0.2}O_{2-\delta}$ as a model catalyst. After each oxidation run, the

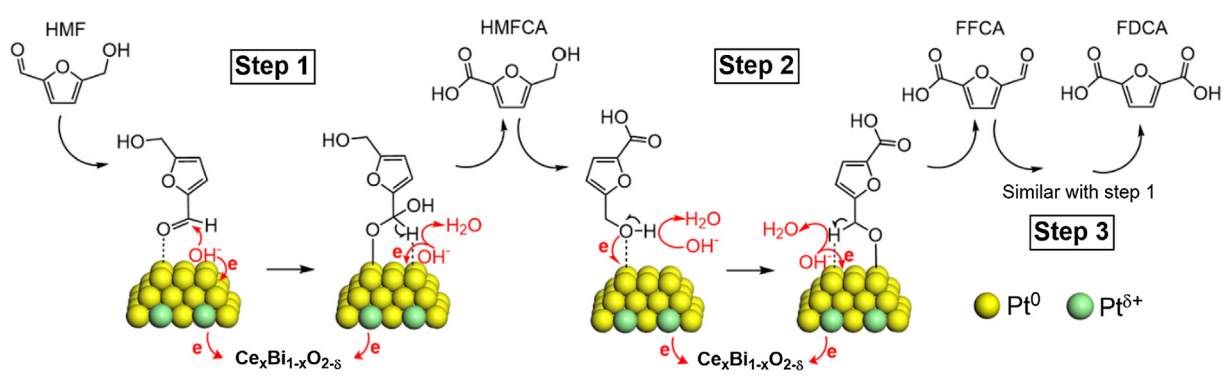

Scheme 1. Proposed mechanism for the oxidation reactions from HMF to FDCA on a Pt/3DOM-$Ce_xBi_{1-x}O_{2-\delta}$ catalyst.

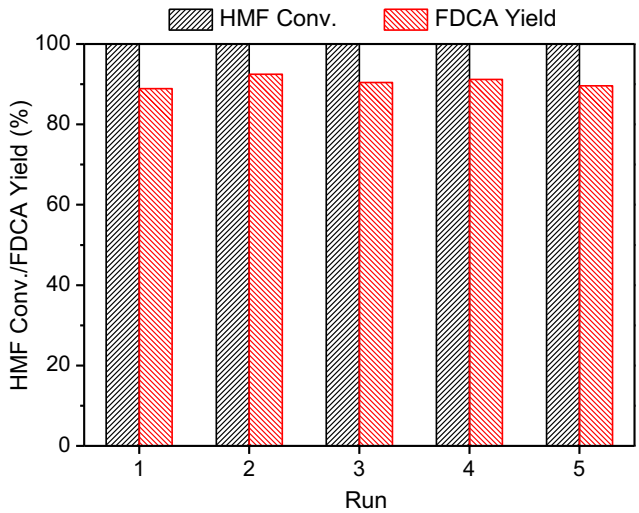

Fig. 12. Recycling tests of Pt/3DOM-$Ce_{0.8}Bi_{0.2}O_{2-\delta}$ for the aerobic oxidation of HMF.

catalyst was recovered by filtration, thoroughly washed with ethanol, and then dried at 50 °C. In order to detect the actual stability of the catalyst, a reaction time of 6 h in each run was chosen, because the oxidation reaction was still in progress at this time. The results of five consecutive cycle experiments are shown in Fig. 12. It can be seen that Pt/3DOM-$Ce_{0.8}Bi_{0.2}O_{2-\delta}$ exhibits excellent reusability in the aerobic oxidation of HMF. In the fifth cycle, 100% HMF conversion and 90% FDCA yield are achieved, which are comparable with the results in the first cycle (100% HMF conversion and 89% FDCA yield). The reaction solution catalyzed by Pt/3DOM-$Ce_{0.8}Bi_{0.2}O_{2-\delta}$ was detected by ICP-AES after centrifuging to separate the catalyst. Only 0.06% Pt leaching was observed in the reaction solution of the first cycle, and no Pt leaching can be detected in the reaction solution of the second cycle. This indicates that the Pt/3DOM-$Ce_{1-x}Bi_xO_{2-\delta}$ catalysts obtained in the present work are stable and can be reused at least five times without any notable loss of catalytic performance.

4. Conclusions

In summary, the principal role of Bi-doping in Pt/3DOM-$Ce_{1-x}Bi_xO_{2-\delta}$ catalysts for the aerobic oxidation of HMF is to form an asymmetric environment of some oxygen vacancies, such as Bi-□(-Ce)$_3$. The chief advantage of these asymmetric clusters, in comparison with symmetric clusters, e.g., (Ce-)$_2$□(-Ce)$_2$ or the clusters containing more than one Bi^{3+} cation, is that both the occupied and unoccupied states at the oxygen sites in these clusters are metastable, making oxygen easy come, easy go. More importantly, in the oxygen adsorption/desorption cycle at these clusters, oxygen molecules are reduced by taking electrons from the Ce^{3+} cations in the clusters, increasing the potential for electron transfer from the Pt nanoparticles to these clusters. It is obvious that the Bi-doping effect on the promotion of catalytic properties is not simply increasing the number of oxygen vacancies, but more importantly, modifying the environment of the oxygen vacancies. We anticipate that this work can shed light on the future investigation of electron transfer between catalytic nanoparticles and oxide substrates, and relevant mechanisms of many other catalytic processes.

Acknowledgments

We thank Professor J.-Q. Yu for a useful discussion. This work was supported by the Tianjin Municipal Natural Science Foundation (Grant 17JCYBJC22600), the China Scholarship Council (Grants 201606200096 and 201606200087), and the Fundamental Research Funds for the Central Universities. Computational support was provided by the Beijing Computing Center (BCC).

References

[1] Y. Lykhach, S.M. Kozlov, T. Skála, A. Tovt, V. Stetsovych, N. Tsud, F. Dvořák, V. Johánek, A. Neitzel, J. Mysliveček, S. Fabris, V. Matolín, K.M. Neyman, J. Libuda, Counting electrons on supported nanoparticles, Nat. Mater. 15 (2016) 284–289.
[2] A. Bruix, J.A. Rodriguez, P.J. Ramírez, S.D. Senanayake, J. Evans, J.B. Park, D. Stacchiola, P. Liu, J. Hrbek, F. Illas, A new type of strong metal-support interaction and the production of H_2 through the transformation of water on Pt/CeO_2(111) and Pt/CeO_x/TiO_2(110) catalysts, J. Am. Chem. Soc. 134 (2012) 8968–8974.
[3] C.T. Campbell, Electronic perturbations, Nat. Chem. 4 (2012) 597–598.
[4] T. Montini, M. Melchionna, M. Monai, P. Fornasiero, Fundamentals and catalytic applications of CeO_2-based materials, Chem. Rev. 116 (2016) 5987–6041.
[5] J. Ke, J.W. Xiao, W. Zhu, H.C. Liu, R. Si, Y.W. Zhang, C.H. Yan, Dopant-induced modification of active site structure and surface bonding mode for high-performance nanocatalysts: CO oxidation on capping-free (110)-oriented CeO_2: Ln (Ln = La–Lu) nanowires, J. Am. Chem. Soc. 135 (2013) 15191–15200.
[6] H.Y. Kim, H.M. Lee, G. Henkelman, CO oxidation mechanism on CeO_2-supported Au nanoparticles, J. Am. Chem. Soc. 134 (2012) 1560–1570.
[7] E. Aneggi, D. Wiater, C. de Leitenburg, J. Llorca, A. Trovarelli, Shape-dependent activity of ceria in soot combustion, ACS Catal. 4 (2014) 172–181.
[8] Y.C. Wei, J. Liu, Z. Zhao, A.J. Duan, G.Y. Jiang, The catalysts of three-dimensionally ordered macroporous $Ce_{1-x}Zr_xO_2$-supported gold nanoparticles for soot combustion: the metal–support interaction, J. Catal. 287 (2012) 13–29.
[9] M.J. Beier, T.W. Hansen, J.-D. Grunwaldt, Selective liquid-phase oxidation of alcohols catalyzed by a silver-based catalyst promoted by the presence of ceria, J. Catal. 266 (2009) 320–330.
[10] M. Tamura, K. Tomishige, Redox properties of CeO_2 at low temperature: the direct synthesis of imines from alcohol and amine, Angew. Chem. Int. Ed. 54 (2015) 864–867.
[11] M.E. Zakrzewska, E. Bogel-Łukasik, R. Bogel-Łukasik, Ionic liquid-mediated formation of 5-hydroxymethylfurfural—a promising biomass-derived building block, Chem. Rev. 111 (2011) 397–417.
[12] R.-J. van Putten, J.C. van der Waal, E. de Jong, C.B. Rasrendra, H.J. Heeres, J.G. de Vries, Hydroxymethylfurfural, a versatile platform chemical made from renewable resources, Chem. Rev. 113 (2013) 1499–1597.
[13] G. Yong, Y. Zhang, J.Y. Ying, Efficient catalytic system for the selective production of 5-hydroxymethylfurfural from glucose and fructose, Angew. Chem. Int. Ed. 47 (2008) 9345–9348.
[14] Z. Zhang, K. Deng, Recent advances in the catalytic synthesis of 2,5-furandicarboxylic acid and its derivatives, ACS Catal. 5 (2015) 6529–6544.
[15] X. Zhang, K. Wilson, A.F. Lee, Heterogeneously catalyzed hydrothermal processing of C5–C6 sugars, Chem. Rev. 116 (2016) 12328–12368.
[16] A.J.J.E. Eerhart, A.P.C. Faaij, M.K. Patel, Replacing fossil based PET with biobased PEF; process analysis, energy and GHG balance, Energy Environ. Sci. 5 (2012) 6407–6422.
[17] O. Casanova, S. Iborra, A. Corma, Biomass into chemicals: aerobic oxidation of 5-hydroxymethyl-2-furfural into 2,5-furandicarboxylic acid with gold nanoparticle catalysts, ChemSusChem 2 (2009) 1138–1144.
[18] Z. Zhang, J. Zhen, B. Liu, K. Lv, K. Deng, Selective aerobic oxidation of the biomass-derived precursor 5-hydroxymethylfurfural to 2,5-furandicarboxylic acid under mild conditions over a magnetic palladium nanocatalyst, Green Chem. 17 (2015) 1308–1317.
[19] X. Han, L. Geng, Y. Guo, R. Jia, X. Liu, Y. Zhang, Y. Wang, Base-free aerobic oxidation of 5-hydroxymethylfurfural to 2,5-furandicarboxylic acid over a Pt/C-O-Mg catalyst, Green Chem. 18 (2016) 1597–1604.
[20] S. Albonetti, A. Lolli, V. Morandi, A. Migliori, C. Lucarelli, F. Cavani, Conversion of 5-hydroxymethylfurfural to 2,5-furandicarboxylic acid over Au-based catalysts: optimization of active phase and metal–support interaction, Appl. Catal. B Environ. 163 (2015) 520–530.
[21] Z. Miao, Y. Zhang, X. Pan, T. Wu, B. Zhang, J. Li, T. Yi, Z. Zhang, X. Yang, Superior catalytic performance of $Ce_{1-x}Bi_xO_{2-\delta}$ solid solution and Au/$Ce_{1-x}Bi_xO_{2-\delta}$ for 5-hydroxymethylfurfural conversion in alkaline aqueous solution, Catal. Sci. Technol. 5 (2015) 1314–1322.
[22] A. Lolli, R. Amadori, C. Lucarelli, M.G. Cutrufello, E. Rombi, F. Cavani, S. Albonetti, Hard-template preparation of Au/CeO_2 mesostructured catalysts and their activity for the selective oxidation of 5-hydroxymethylfurfural to 2,5-furandicarboxylic acid, Micropor. Mesopor. Mater. 226 (2016) 466–475.
[23] Z. Miao, T. Wu, J. Li, T. Yi, Y. Zhang, X. Yang, Aerobic oxidation of 5-hydroxymethylfurfural (HMF) effectively catalyzed by a $Ce_{0.8}Bi_{0.2}O_{2-\delta}$ supported Pt catalyst at room temperature, RSC Adv. 5 (2015) 19823–19829.
[24] K. Yu, C. Zhang, Y. Chang, Y. Feng, Z. Yang, T. Yang, L.-L. Lou, S. Liu, Novel three-dimensionally ordered macroporous $SrTiO_3$ photocatalysts with remarkably enhanced hydrogen production performance, Appl. Catal. B Environ. 200 (2017) 514–520.
[25] G. Kresse, J. Furthmüller, Efficiency of *ab-initio* total energy calculations for metals and semiconductors using a plane-wave basis set, Comput. Mater. Sci. 6 (1996) 15–50.

[26] G. Kresse, J. Furthmüller, Efficient iterative schemes for *ab initio* total-energy calculations using a plane-wave basis set, Phys. Rev. B 54 (1996) 11169–11186.
[27] J.P. Perdew, Y. Wang, Accurate and simple analytic representation of the electron-gas correlation energy, Phys. Rev. B 45 (1992) 13244–13249.
[28] Z. Yang, Q. Wang, S. Wei, D. Ma, Q. Sun, The effect of environment on the reaction of water on the ceria(111) surface: a DFT+U study, J. Phys. Chem. C 114 (2010) 14891–14899.
[29] C. Loschen, J. Carrasco, K.M. Neyman, F. Illas, First-principles LDA+U and GGA +U study of cerium oxides: dependence on the effective U parameter, Phys. Rev. B 75 (2007) 5115.
[30] M. Nolan, S. Grigoleit, D.C. Sayle, S.C. Parker, G.W. Watson, Density functional theory studies of the structure and electronic structure of pure and defective low index surfaces of ceria, Surf. Sci. 576 (2005) 217–229.
[31] S. Fabris, S. de Gironcoli, S. Baroni, G. Vicario, G. Balducci, Taming multiple valency with density functionals: a case study of defective ceria, Phys. Rev. B. 71 (2005) 1102–1105.
[32] W.Z. Zhou, Defect fluorite–related superstructures in the Bi_2O_3–V_2O_5 system, J. Solid State Chem. 76 (1988) 290–300.
[33] X.-M. Zhang, Y.-Q. Deng, P. Tian, H.-H. Shang, J. Xu, Y.-F. Han, Dynamic active sites over binary oxide catalysts: *in situ*/operando spectroscopic study of low-temperature CO oxidation over MnO_x-CeO_2 catalysts, Appl. Catal. B Environ. 191 (2016) 179–191.
[34] S. Ramana, B.G. Rao, P. Venkataswamy, A. Rangaswamy, B.M. Reddy, Nanostructured Mn-doped ceria solid solutions for efficient oxidation of vanillyl alcohol, J. Mol. Catal. A Chem. 415 (2016) 113–121.
[35] Y. Zhang, Y. Yang, J. Zheng, W. Hua, G. Chen, Effects of oxidizing additives on optical properties of Bi_2O_3–B_2O_3–SiO_2 glasses, J. Am. Ceram. Soc. 91 (2008) 3410–3412.
[36] F. Schröder, N. Bagdassarov, F. Ritter, L. Bayarjargal, Temperature dependence of Bi_2O_3 structural parameters close to the α–δ phase transition, Phase Transit. 83 (2010) 311–325.
[37] M. Guo, J. Lu, Y. Wu, Y. Wang, M. Luo, UV and visible Raman studies of oxygen vacancies in rare-earth-doped ceria, Langmuir 27 (2011) 3872–3877.
[38] M.A. Henderson, C.L. Perkins, M.H. Engelhard, S. Thevuthasan, C.H.F. Peden, Redox properties of water on the oxidized and reduced surfaces of CeO_2(111), Surf. Sci. 526 (2003) 1–18.
[39] L. Óvári, S. Krick Calderon, Y. Lykhach, J. Libuda, A. Erdőhelyi, C. Papp, J. Kiss, H.-P. Steinrück, Near ambient pressure XPS investigation of the interaction of ethanol with Co/CeO_2(111), J. Catal. 307 (2013) 132–139.
[40] S. Zhan, H. Zhang, Y. Zhang, Q. Shi, Y. Li, X. Li, Efficient NH_3-SCR removal of NO_x with highly ordered mesoporous $WO_3(\chi)$-CeO_2 at low temperatures, Appl. Catal. B Environ. 203 (2017) 199–209.
[41] N. Jabeen, Q. Xia, S.V. Savilov, S.M. Aldoshin, Y. Yu, H. Xia, Enhanced pseudocapacitive performance of α-MnO_2 by cation preinsertion, ACS Appl. Mater. Inter. 8 (2016) 33732–33740.
[42] S.M. Kozlov, K.M. Neyman, Effects of electron transfer in model catalysts composed of Pt nanoparticles on CeO_2(111) surface, J. Catal. 344 (2016) 507–514.
[43] W.Z. Zhou, Defect fluorite superstructures in the Bi_2O_3–WO_3 system, J. Solid State Chem. 108 (1994) 381–394.
[44] J. Yang, C.-Q. Lv, Y. Guo, G.-C. Wang, A DFT+U study of acetylene selective hydrogenation on oxygen defective anatase (101) and rutile (110) TiO_2 supported Pd4 cluster, J. Chem. Phys. 136 (2012) 104107.
[45] Y. Wang, K. Yu, D. Lei, W. Si, Y. Feng, L.-L. Lou, S. Liu, Basicity-tuned hydrotalcite-supported Pd catalysts for aerobic oxidation of 5-hydroxymethyl-2-furfural under mild conditions, ACS Sust. Chem. Eng. 4 (2016) 4752–4761.
[46] D. Lei, K. Yu, M.-R. Li, Y. Wang, Q. Wang, T. Liu, P. Liu, L.-L. Lou, G. Wang, S. Liu, Facet effect of single-crystalline Pd nanocrystals for aerobic oxidation of 5-hydroxymethyl-2-furfural, ACS Catal. 7 (2017) 421–432.
[47] S. Siankevich, G. Savoglidis, Z. Fei, G. Laurenczy, D.T.L. Alexander, N. Yan, P.J. Dyson, A novel platinum nanocatalyst for the oxidation of 5-hydroxymethylfurfural into 2,5-furandicarboxylic acid under mild conditions, J. Catal. 315 (2014) 67–74.
[48] H. Ait Rass, N. Essayem, M. Besson, Selective aqueous phase oxidation of 5-hydroxymethylfurfural to 2,5-furandicarboxylic acid over Pt/C catalysts: influence of the base and effect of bismuth promotion, Green Chem. 15 (2013) 2240–2251.
[49] H. Ait Rass, N. Essayem, M. Besson, Selective aerobic oxidation of 5-HMF into 2,5-furandicarboxylic acid with Pt catalysts supported on TiO_2- and ZrO_2-based supports, ChemSusChem 8 (2015) 1206–1217.
[50] R.F.W. Bader, Atoms in Molecules—A Quantum Theory, Oxford University Press, New York, 1990.
[51] G. Henkelman, A. Arnaldsson, H. Jónsson, A fast and robust algorithm for bader decomposition of charge density, Comput. Mater. Sci. 36 (2006) 354–360.
[52] D. Guo, G.-C. Wang, Partial oxidation of methane on anatase and rutile defective TiO_2 supported Rh4 cluster: a density functional theory study, J. Phys. Chem. C 121 (2017) 26308–26320.
[53] S.E. Davis, B.N. Zope, R.J. Davis, On the mechanism of selective oxidation of 5-hydroxymethylfurfural to 2,5-furandicarboxylic acid over supported Pt and Au catalysts, Green Chem. 14 (2012) 143–147.
[54] B.N. Zope, D.D. Hibbitts, M. Neurock, R.J. Davis, Reactivity of the gold/water interface during selective oxidation catalysis, Science 330 (2010) 74–78.
[55] Y.M. Choi, H. Abernathy, H.-T. Chen, M.C. Lin, M. Liu, Characterization of O_2-CeO_2 interactions using *in situ* Raman spectroscopy and first-principle calculations, ChemPhysChem 7 (2006) 1957–1963.
[56] S.E. Davis, L.R. Houk, E.C. Tamargo, A.K. Datye, R.J. Davis, Oxidation of 5-hydroxymethylfurfural over supported Pt, Pd and Au catalysts, Catal. Today 160 (2011) 55–60.